Control Strategy and Modulation Scheme of Three-Phase Quasi-Single-Stage Isolated AC–DC Converter Based on Dual Active Bridge

Luming Liu and Zhiqiang Guo, *Senior Member, IEEE*

***Abstract*—This article proposes a three-phase quasi-single-stage isolated ac–dc converter, comprising a hybrid active third-harmonic injection buck-type rectifier (H3R) and a dual active bridge (DAB). Based on the input current analysis, globally optimal working modes of the DAB converter are derived through optimal triple-phase-shift (TPS) modulation, minimizing conduction losses while achieving wide-range zero-voltage switching (ZVS). A voltage-current closed-loop control strategy is proposed to regulate the output voltage and precisely control both the input current and third-harmonic injection current, achieving unity power factor (PF). This proposed approach eliminates the dc-link capacitor. By implementing the shared controller between the ac–dc and dc–dc stages, the quasi-single-stage topology simplifies control complexity while providing the PF correction and stable dc output voltage. Furthermore, the transformer and inductor parameters in the DAB converter are optimized through a genetic algorithm (GA) to minimize total loss, further improving the converter efficiency. Finally, a 1.6-kW experimental prototype with 200 V/50 Hz input line-to-line voltage and 200 V/250 V output voltage is built to validate the effectiveness and advantage of the proposed topology and control strategy.**

***Index Terms*—Active third-harmonic injection, dual active bridge, quasi-single-stage isolated ac–dc converter, unit power factor.**

I. Introduction

With the development of energy storage systems and electric vehicles, particularly the increasing maturity of vehicle-to-grid and vehicle-to-building technologies, the high-efficiency isolated bidirectional ac–dc converters have become critical components in modern power conversion infrastructure [1], [2], [3]. The conventional isolated ac–dc converters typically employ a multistage power conversion architecture: a front-end ac–dc stage performing power factor correction (PFC), an intermediate dc bus, and a rear-stage high-frequency isolated dc–dc converter for voltage regulation [4], [5]. Although this configuration can decouple input ac characteristics from output voltage control, the inherent structural complexity and lower power conversion efficiency of multistage architectures notably increase system volume and cost. Consequently, the single-stage isolated ac–dc converters, which eliminate the intermediate dc-link stage and exhibit notable advantages in power density and efficiency, have attracted increasing attention in recent research [6], [7].

In recent years, researchers have achieved substantial progress in topologies and control strategies for single-stage isolated ac–dc converters. Generally, these topologies can be classified into two categories. The first category of topologies, such as the matrix-type converters, which achieve single-stage power conversion with full high-frequency switching operation. In [8], a novel single-stage isolated matrix-type converter topology is developed for offshore wind systems, eliminating the bidirectional switches to enhance reliability and reduce conduction loss. To improve the system scalability and wide input voltage operation, the modular isolated matrix-type converters are introduced in [9], [10]. Nevertheless, the modular structure imposes considerable complexity on the coordinated control of parallel modules under load variations. For the modulation schemes, several asymmetrical SVPWM schemes are developed in [11] for the fault-tolerant operation of matrix-type converters. However, the operation range is severely limited. In order to expand the operation range while reducing the switching actions and switching loss, a quasi-symmetrical SVPWM technique is introduced in [12], though it requires accurate modeling. To achieve minimum current stress, the relationship between the modulation index and phase shift angle is derived from the transferred power model for real-time duty cycle control [13], [14]. However, the fixed duty cycle in these coordinating control methods inherently limits global optimization, resulting in higher power loss and lower efficiency. Based on the trapezoidal waveform modulation (TZM) techniques, a dual-period space vector modulation (SVM) scheme is proposed in [15] for transformer currents decoupling, which effectively reduces low-order harmonics of the ac-side current. Nevertheless, this strategy limits the maximum transfer power. In addition, TZM causes the converter to fail to achieve zero-voltage switching (ZVS), resulting in higher switching losses and lower efficiency. To improve the maximum transfer power and the system power density, a variable switching period based dual-period SVM scheme is developed in [16].

Received 19 August 2025; revised 18 November 2025; accepted 8 January 2026. Date of publication 13 January 2026; date of current version 20 March 2026. This work was supported in part by the National Natural Science Foundation of China under Grant 52477174 and in part by the State Key Laboratory of Power System Operation and Control under Grant SKLD24KM29. Recommended for publication by Associate Editor K. Gunawardane. *(Corresponding author: Zhiqiang Guo.)*

The authors are with the School of Automation, Beijing Institute of Technology, Beijing 100081, China (e-mail: liuluming@bit.edu.cn; guozq32@bit.edu.cn).

Color versions of one or more figures in this article are available at https://doi.org/10.1109/TPEL.2026.3653803.

Digital Object Identifier 10.1109/TPEL.2026.3653803

However, this method still disables ZVS operation. In [17], an efficiency-optimization control strategy to suppress the transient dc bias current is proposed, achieving ZVS and reducing turn-ON switching loss. A three-phase single-stage matrix-type *LCL* resonant ac–dc converter is proposed in [18]. The *LCL* resonant tank is supplied by a five-level voltage generated from the matrix converter. Based on this, the optimal modulation strategy is developed by combining the analytical expressions of the input current with the modified ZVS conditions, thereby simplifying the control complexity and improving the conversion efficiency. To enhance the system conversion efficiency, dual active bridge (DAB)-based matrix-type converters with the novel modulation strategies are proposed in [19], [20]. These methods achieve soft-switching for all semiconductor devices. Further improving the design, accurate loss models for the three-phase isolated matrix-type converters are elaborated in [21], [22]. These works effectively reduce circuit loss while lowering the circuit cost. To mitigate the low-order harmonics and improve the current quality, an improved SVM strategy is introduced in [23] to reallocate the duty cycle of zero vectors and switching sequence, reducing the switching actions and the low-order harmonics.

Owing to advancements in rectifier technology, single-stage isolated ac–dc converters based on rectifier topologies have been widely discussed [2]. In the second category of topologies, the switches of the front-end non-isolated rectifier typically operate at a low switching frequency to facilitate current commutation. Furthermore, eliminates the dc-link capacitor for energy storage, and the PFC is performed by the subsequent isolated dc–dc converter. Compared to single-stage matrix-type ac–dc converters, these topologies offer simpler and more flexible control while achieving higher efficiency. The SWISS rectifier is a popular solution for single-stage isolated ac–dc converters. The conventional SWISS rectifier allows only for unidirectional power flow [24]. To achieve bidirectional power transfer, the bidirectional SWISS rectifier is developed [25], [26]. In [27], two phase-shifted full-bridge (PSFB) converters are connected to the output of the SWISS rectifier to construct an isolated single-stage ac–dc converter. However, this redundant and complex structure leads to higher power losses. To improve the efficiency and power density, an optimized topology based on a single full-bridge (SFB) with a midpoint-clamper is presented in [28]. Although the optimized topology reduces the volume and loss, it limits the soft-switching range. In [29], a series-parallel *LLC* resonant structure is developed to replace SFB, achieving wide-range soft switching. Nevertheless, bidirectional power transfer has not been realized in all these topologies. Furthermore, although significant advancements in control flexibility have been made, the efficiency and power density still require substantial improvement. As an outstanding rectifier topology, the hybrid active third-harmonic injection buck-type rectifier (H3R) features higher efficiency and lower current stress [30], [31]. A comprehensive comparison of the performance of H3R with the SWISS rectifier and other rectifiers is presented in [25], which concludes that H3R is the most advantageous topology. It has been widely applied in many power electronic applications such as more electric aircraft, ac–ac systems, and variable-speed ac drives [31], [32], [33]. However, the research on this topology in single-stage isolated ac–dc converters remains relatively scarce.

In this article, a three-phase quasi-single-stage isolated bidirectional ac–dc converter is proposed, formed by coupling a DAB converter to the output stage of the H3R. Owing to the advantages of DAB converters in bidirectional power flow and wide voltage conversion ratio, it has been widely adopted in isolated bidirectional power conversion [34], [35], [36], [37], [38], [39]. However, achieving minimum conduction loss while maintaining wide-range ZVS still remains challenging under the fluctuating input voltage. In addition, for DAB-based single-stage ac–dc converters, the conversion ratio is varied with the pulsating input voltage in a very wide range. This poses a significant challenge for distributing the optimal working modes of the DAB converter over a line-frequency period. The main contributions of this article are as follows.

1) A voltage-current closed-loop cooperative control strategy is proposed for the quasi-single-stage isolated ac–dc converter to regulate the output voltage and the input ac power quality.
2) A globally optimized triple-phase-shift (TPS) modulation strategy is proposed to simultaneously minimize conduction loss and realize wide-range ZVS operation under the pulsating input voltage. Furthermore, the relationship among the ac input current, the H3R auxiliary bridge current, and the DAB input current is derived, which allows the DAB input current to be directly controlled by the TPS modulation strategy, thereby achieving precise control of the ac input current.
3) The parameters of magnetic components, such as the series inductance and transformer turns ratio, critically influence the converter efficiency. However, these parameters are difficult to determine directly through analytical methods. To address this limitation, a numerical optimization method based on genetic algorithm (GA) is proposed for optimal design of the magnetic components, thereby further improving the conversion efficiency.

The rest of this article is organized as follows. Section II introduces the working principles of the proposed topology, analyzes the input current of the DAB converter under unity PF operation, and discusses the power flow characteristics. Section III deduces the optimal working mode of the DAB converter and proposes the modulation scheme and control strategy for the three-phase quasi-single-stage isolated ac–dc converter. Section IV presents the loss analysis and derives the optimal parameters that minimize the total loss. Then, the experimental results are presented in Section V to verify the effectiveness of the proposed solution. Finally, Section VI concludes this article.

II. Working Principles of the Three-phase Quasi-Single-Stage Isolated AC–DC Converter

A. Topology and Working Principles

The topology of the three-phase quasi-single-stage isolated bidirectional H3R ac–dc converter based on DAB is shown in Fig. 1, which consists of an input voltage sector (IVS), a bridge arm for third-harmonic current injection control (Y-bridge arm),

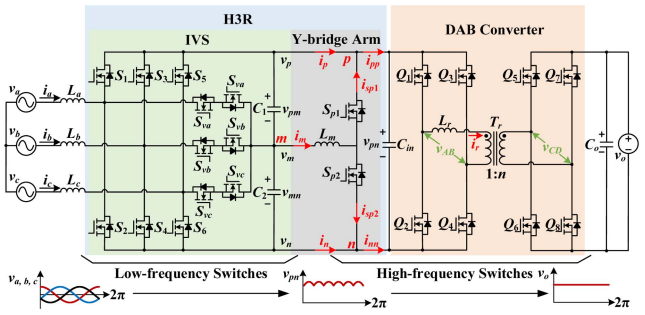

Fig. 1. Topology of the three-phase quasi-single-stage isolated bidirectional H3R AC–DC converter based on DAB.

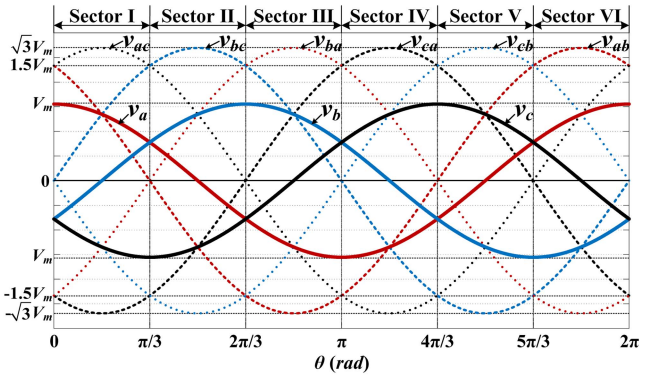

Fig. 2. Three-phase input voltage and sector division.

and a DAB converter. The IVS is composed of a three-phase fully-controlled bridge (S_1–S_6) and three bidirectional switches (S_{va}, S_{vb}, and S_{vc}). The switches of IVS are all low-frequency switches. The Y-bridge arm includes a third-harmonic injection inductor L_m and two switches (S_{p1}, S_{p2}). Unlike the standard two-stage ac–dc converters, the filter capacitors C_1, C_2, and C_3 in this topology are not employed to maintain a constant dc-link voltage but cooperate with the ac-side inductors L_a , L_b, and L_c to implement an LC filter to suppress the high-frequency component of the input currents. Therefore, the capacitances are very small.

The ac-side voltage is shown in Fig. 2. According to the instantaneous value of three-phase ac voltage v_a, v_b, and v_c, one line frequency cycle is divided into six sectors. Within each sector, only one group of bidirectional switches is selected and conducted to inject the third-harmonic current into its corresponding input phase voltage. The upper switches (S_1, S_3, or S_5) of the IVS are turned ON for the phase with the maximum instantaneous voltage; the lower switches (S_2, S_4, or S_5) of the IVS are turned ON for the phase with the minimum instantaneous voltage; the bidirectional switches (S_{va}, S_{vb}, or S_{vc}) of the IVS are turned ON for the median instantaneous phase voltage. The switches S_{p1} and S_{p2} of the Y-bridge arm are controlled to generate the third-harmonic current i_m. All the low-frequency driving signals for IVS are presented in Table I. With this gate signal sequence, the H3R outputs a sixfold line-frequency fluctuating dc voltage v_{pn}, which is shown in Fig. 3(a). Then,

TABLE I
MODULATION OF THE H3R

Sector	Switching States									v_{pn}	v_{mn}
	S_1	S_2	S_3	S_4	S_5	S_6	S_{va}	S_{vb}	S_{vc}		
I	1	0	0	0	0	1	0	1	0	v_{ac}	v_{bc}
II	0	0	1	0	0	1	1	0	0	v_{bc}	v_{ac}
III	0	1	1	0	0	0	0	0	1	v_{ba}	v_{ca}
IV	0	1	0	0	1	0	0	1	0	v_{ca}	v_{ba}
V	0	0	0	1	1	0	1	0	0	v_{cb}	v_{ab}
VI	1	0	0	1	0	0	0	0	1	v_{ab}	v_{cb}

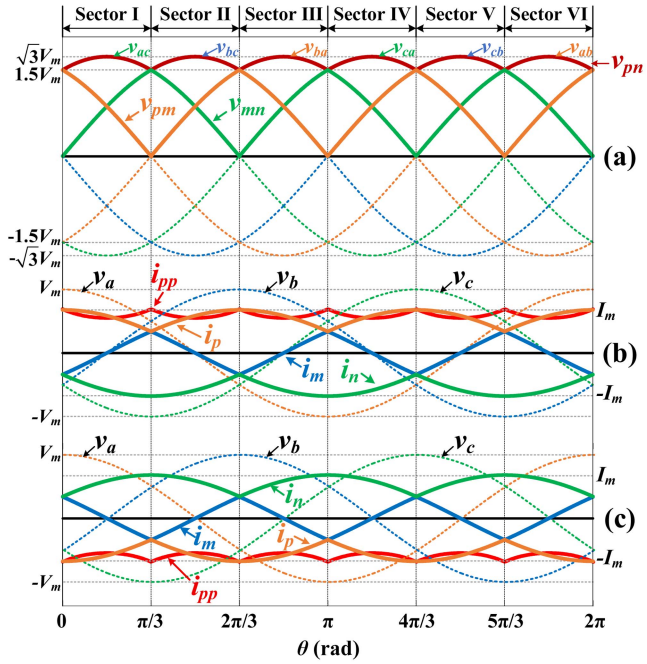

Fig. 3. Typical waveforms in the H3R. (a) Output voltage waveforms of the H3R. (b) Current waveforms in rectifying mode. (c) Current waveforms in inverting mode.

the DAB converter transforms v_{pn} into the constant dc output voltage v_o.

B. Current Analysis and Control

As shown in Fig. 2, the three-phase ac supply is assumed as an ideal source. The distortion-free three-phase voltages can be expressed by (1) under unity PF conditions

$$\begin{cases} v_a = V_m \cos(\theta) \\ v_b = V_m \cos(\theta - 2\pi/3) \\ v_c = V_m \cos(\theta + 2\pi/3) \end{cases} \tag{1}$$

where θ is the phase angle, and V_m is the amplitude of the three-phase voltage.

To further analyze the output voltage of H3R, the three-phase input voltages are ranked according to their instantaneous values in each sector

$$\begin{cases} v_{\max} = \max(v_a, v_b, v_c) \\ v_{\text{mid}} = \text{mid}(v_a, v_b, v_c) \\ v_{\min} = \min(v_a, v_b, v_c) \end{cases} \tag{2}$$

where $v_{\max}$, v_{mid}, and $v_{\min}$ are denoted the maximum, median, and minimum values of the three-phase voltage, respectively.

Then, according to the working principles described in Section II-A, the output voltages of H3R can be expressed in the following equation:

$$\begin{cases} v_{pn} = v_{\max} - v_{\min} \\ v_{pm} = v_{\max} - v_{\mathrm{mid}} \\ v_{mn} = v_{\mathrm{mid}} - v_{\min} \end{cases}. \tag{3}$$

v_{pn}, v_{pm}, and v_{mn} in each sector are also presented in Table I and described in Fig. 3(a).

To ensure the three-phase input currents are sinusoidal, precise control of third-harmonic current injection is essential. Under the constraints that the volt-second integral should be zero over a whole switching cycle, the duty cycles of the switches S_{p1} and S_{p2} could be derived from the voltage-second balance of the third-harmonic injection inductor L_m

$$\begin{cases} v_{pm} \cdot D_{p1} - v_{mn} \cdot D_{p2} = 0 \\ D_{p1} + D_{p2} = 1 \end{cases} \tag{4}$$

where D_{p1} and D_{p2} are the theoretical duty cycles of the switches S_{p1} and S_{p2} in the Y-bridge arm, respectively. Then, the duty cycles are solved in the following equation:

$$\begin{cases} D_{p1} = \frac{v_{mn}}{v_{pm}+v_{mn}} = \frac{v_{mn}}{v_{pn}} \\ D_{p2} = \frac{v_{pm}}{v_{pm}+v_{mn}} = \frac{v_{pm}}{v_{pn}} \end{cases}. \tag{5}$$

To achieve a unity PF, the currents must be in phase with corresponding voltages in rectifying mode, whereas a 180° phase shift is required between currents and voltages during inverting operation. To facilitate further analysis, this paper focuses on the analysis of forward power. The inverting operation can be analyzed in the same method. Thus, the three-phase currents are expressed as follows in the rectifying mode:

$$\begin{cases} i_a = I_m \cos(\theta) \\ i_b = I_m \cos(\theta - 2\pi/3) \\ i_c = I_m \cos(\theta + 2\pi/3) \end{cases} \tag{6}$$

where I_m is the amplitude of the three-phase currents.

According to the switching logic shown in Table I, the currents i_p, i_m, and i_n defined in Fig. 1 should be controlled as follows:

$$\begin{cases} i_p = \max\{i_a, i_b, i_c\} \\ i_m = \mathrm{mid}\{i_a, i_b, i_c\} \\ i_n = \min\{i_a, i_b, i_c\} \end{cases}. \tag{7}$$

Based on the sector division in Fig. 3, the duty cycles D_{p1} and D_{p2} can be obtained from (5) for each sector. Then, the average currents in switches S_{p1} and S_{p2}, denoted i_{sp1} and i_{sp2}, which are shown in Fig. 1, can be expressed in the following equation:

$$\begin{cases} i_{sp1} = D_{p1} \cdot i_m = \frac{v_{mn}}{v_{pn}} \cdot i_m \\ i_{sp2} = D_{p2} \cdot i_m = \frac{v_{pm}}{v_{pn}} \cdot i_m \end{cases} \tag{8}$$

where i_m is the third-harmonic current.

And the input current of the DAB converter i_{pp} is presented as

$$i_{pp} = i_p + i_{sp1}. \tag{9}$$

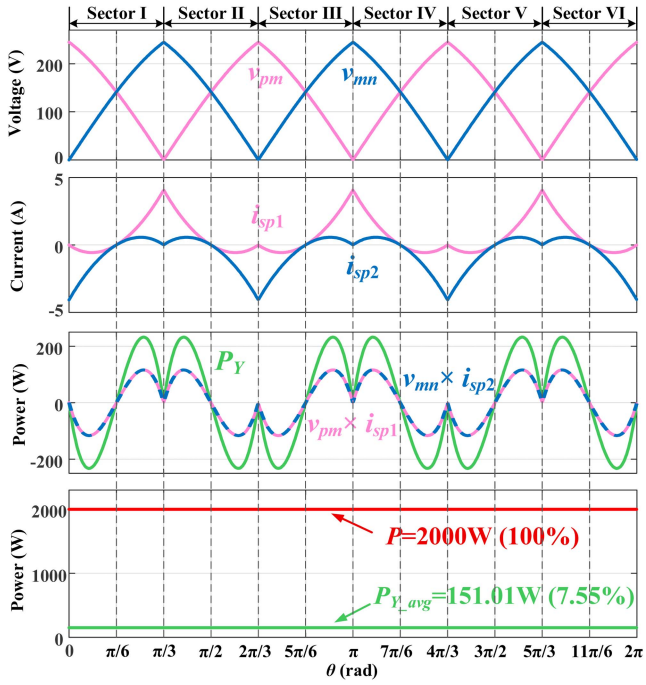

Fig. 4. Power analysis and comparison.

In summary, as shown in Fig. 3, when the currents i_p and i_n and third-harmonic injection current i_m are all properly regulated, the sinusoidal three-phase input currents and unity PF are attainable.

C. Power Analysis and Comparison

As shown in Fig. 3(b) and (8), the currents i_m, i_{sp1}, and i_{sp2} share identical magnitudes at half the phase current amplitude, resulting in low power loss in the Y-bridge arm. Furthermore, according to the conduction logic shown in Table I, the three-phase fully-controlled bridge switches (S_1–S_6) operate at line frequency, and the bidirectional switches (S_{va}, S_{vb}, and S_{vc}) operate at twice the line frequency. This means switching loss in the IVS can be ignored.

To gain a deeper insight into the power flow characteristics and the power distribution, the instantaneous power P_Y handled by the Y-bridge arm is expressed in the following equation:

$$P_Y = v_{pm} \cdot i_{sp1} + v_{mn} \cdot i_{sp2}. \tag{10}$$

The symmetrical waveform of instantaneous power P_Y is shown in Fig. 4, which exhibits balanced positive and negative values over a sector period. This demonstrates that the Y-bridge arm handles purely circulating power, resulting in zero net active power transfer within a line frequency cycle.

To quantitatively analyze the proportion of power processed by the Y-bridge arm, the average value of circulating power P_Y is expressed as follows:

$$P_{Y\_\mathrm{avg}} = \frac{1}{2\pi} \int_0^{2\pi} |P_Y| d\theta. \tag{11}$$

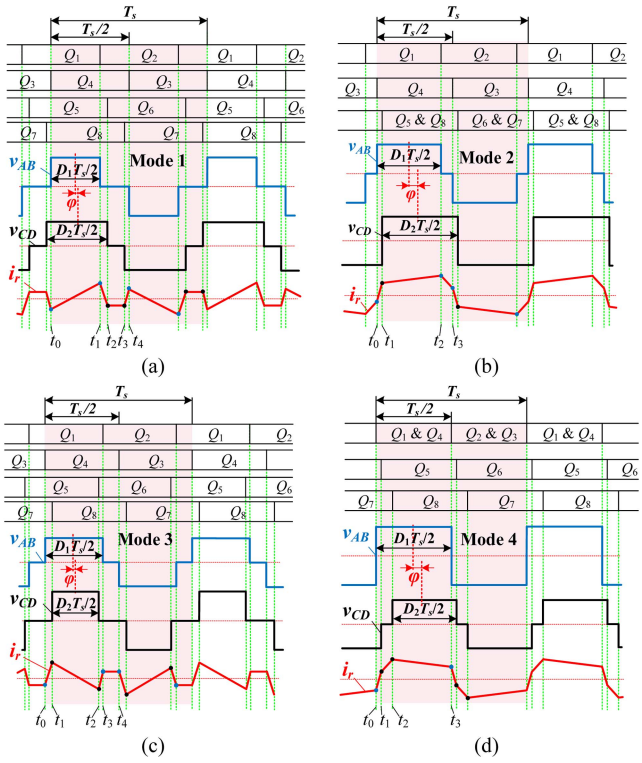

Fig. 5. Key waveforms of TPS. (a) Mode 1. (b) Mode 2. (c) Mode 3. (d) Mode 4.

Assuming the total output power $P = 2$ kW, the calculated $P_{Y\text{-}\mathrm{avg}}$ is only 151.01 W. This indicates that the Y-bridge arm handles very small power, accounting for merely 7.55% of the total power. Consequently, the proposed topology can be considered as the quasi-single-stage solution.

III. Control Strategy and Performance Analyses

A. Optimal Working Modes for DAB Converter

TPS modulation for the DAB converter can achieve global optimization with minimum conduction loss and wide-range ZVS operation [36]. The typical optimal working modes of the DAB converter in forward power flow are presented in Fig. 5. The conversion ratio is defined as $M = v_o/(n{\cdot}v_{in})$, where v_{in} and v_o are denoted as the DAB input and output voltages, respectively. In the H3R ac–dc converter shown in Fig. 3, $v_{in} = v_{pn}$. D_1, D_2, and φ represent duty cycles and phase shift angle of the two full bridges, with $\varphi{\in}[-\pi/2, \pi/2]$. Furthermore, when $\varphi > 0$, the DAB operates in forward power flow; when $\varphi < 0$, it operates in reverse power flow. Due to the symmetry of the bidirectional power flow with opposite phase shift angle, the key waveforms of reverse power flow are not presented. When the conversion ratio $M < 1$, the DAB operates in Mode 1 and Mode 2 as shown in Fig. 5(a) and (b); when $M \geq 1$, it operates in Mode 3 and Mode 4 as shown in Fig. 5(c) and (d).

To achieve high efficiency, low current stress, and wide-range ZVS, the minimum peak current in the series inductor and ZVS conditions of the switches (Q_1–Q_8) are established as the optimization objectives, which are expressed in (12). It is required that the peak current approach the minimum value while meeting the load power demand p^*. Meanwhile, the current magnitude in the series inductor must be sufficient at commutation time to achieve ZVS for all switches

$$\begin{cases} \mathrm{Min}\, i_{\mathrm{peak}}(D_1, D_2, \varphi, v_{in}, v_o) \\ \mathrm{Subject\ to}\, P(D_1, D_2, \varphi, v_{in}, v_o) = p* \\ |i_r(Q_1 - Q_8)| \geq I_{\mathrm{ZVS1}} \text{ or } I_{\mathrm{ZVS2}} \end{cases}. \tag{12}$$

I_{ZVS1} and I_{ZVS2} are the minimum current amplitudes for ZVS of the switches $Q_{1\text{–}4}$ and $Q_{5\text{–}8}$, respectively, which are required to fully charge and discharge junction capacitors of the switches during the dead time [36]. Thus, based on the constant of (12), the transformer current at the turn-ON time (t_x) of the corresponding switches should meet $|i_r(t_x)| \geq I_{\mathrm{ZVS1}}$ or $|i_r(t_x)| \geq I_{\mathrm{ZVS2}}$. If the nonlinear behavior of junction capacitors is ignored, I_{ZVS1} and I_{ZVS2} can be approximately evaluated as $I_{\mathrm{ZVS1}} = 2v_{in}C_{\mathrm{oss1}}/t_{\mathrm{dead}}$ and $I_{\mathrm{ZVS2}} = 2v_oC_{\mathrm{oss2}}/t_{\mathrm{dead}}$, where C_{oss1} represents the output capacitance of $Q_{1\text{–}4}$, C_{oss2} represents the output capacitance of $Q_{5\text{–}8}$, and t_{dead} is the dead time.

Consequently, soft-switching can be achieved for the four optimal modes by modulating D_1, D_2, and φ, thereby reducing the power loss and current stress. The phase shift angle and duty cycles in these four optimal modes are derived in the following.

1) Model 1: The input current and voltage of the DAB converter shown in Fig. 1 are defined as i_{pp} and v_{pn}, respectively. According to the previous study [37], the input current i_{pp} for the forward and reverse power flow is expressed as (13), where $\varphi_s = |2\varphi/\pi|$

$$|i_{pp}| = \frac{P_o}{v_{pn}} = \frac{v_oT_s}{8nL_r}2D_1\varphi_s. \tag{13}$$

Based on the analysis in Section II, when the converter operates at unity PF, the input current can be expressed in (14) by substituting (6), (7), and (8) into (9)

$$\begin{aligned} i_{pp} = i_p + i_{sp1} = I_m max\{\cos(\theta), \cos(\theta - 2\pi/3), \cos(\theta + 2\pi/3)\} \\ + I_m mid\{\cos(\theta), \cos(\theta - 2\pi/3), \cos(\theta + 2\pi/3)\}\frac{v_{mn}}{v_{pn}}. \end{aligned} \tag{14}$$

Defining $I_{\mathrm{base}} = v_oT_s/(8nL_r)$, the amplitude of the three-phase currents in per unit (p.u.) is defined as y, which is expressed as I_m/I_{base}. Thus, the normalized value of DAB input current i_{pp} can be defined as $y_{pp} = i_{pp}/I_{\mathrm{base}}$, which is expressed in (15). According to Fig. 3 and (14), the normalized currents y_{pp} and y share the same range of $[-1, 1]$ under the bidirectional power flow operation

$$\begin{aligned} y_{pp} = y \cdot max\{\cos(\theta), \cos(\theta - 2\pi/3), \cos(\theta + 2\pi/3)\} \\ + y \cdot mid\{\cos(\theta), \cos(\theta - 2\pi/3), \cos(\theta + 2\pi/3)\}\frac{v_{mn}}{v_{pn}}. \end{aligned} \tag{15}$$

Then, (13) can be rewritten in the following equation:

$$|y_{pp}| = 2D_1\varphi_s. \tag{16}$$

According to the optimization objectives presented in (12), the duty cycle expressions of Mode1 in optimal TPS modulation

can be solved by the Karush-Kuhn-Tucker (KKT) method [37]

$$\begin{cases} D_1 = \frac{M}{1-M}\left(\varphi_s + \frac{4nL_rI_{ZVS1}}{v_oT_s}\right) \\ D_2 = \frac{D_1}{M} + \frac{4n^2L_rI_{ZVS2}}{v_oT_s} \end{cases}. \tag{17}$$

Substituting (17) into (16), the phase shift angle can be expressed as follows:

$$\varphi_s = \sqrt{\left(\frac{2nL_rI_{ZVS1}}{v_oT_s}\right)^2 + \frac{1-M}{2M}|y_{pp}|} - \frac{2nL_rI_{ZVS1}}{v_oT_s}. \tag{18}$$

By substituting (18) into (17), the working mode and modulation parameters of the DAB converter can be determined through controlling the normalized input current y_{pp}.

2) Model 2: Similarly, referring to the previous study [37], the input current can be expressed as (19) when the converter works in Model 2

$$|i_{pp}| = \frac{P_o}{v_{pn}} = \frac{v_oT_s}{8nL_r}\left(2\varphi_s - D_1^2 + 2D_1 - {\varphi_s}^2 - 1\right). \tag{19}$$

Similar to Mode 1, (19) can be rewritten in the following equation:

$$|y_{pp}| = 2\varphi_s - D_1^2 + 2D_1 - {\varphi_s}^2 - 1. \tag{20}$$

The duty cycles D_1 and D_2 can be derived by solving (12)

$$\begin{cases} D_1 = \frac{2M-1}{M} + \frac{1-M}{M}\varphi_s \\ D_2 = 1 \end{cases}. \tag{21}$$

Substituting (21) into (20), the phase shift angle is expressed as follows:

$$\varphi_s = 1 - \sqrt{\frac{1-|y_{pp}|}{2 - 2/M + 1/M^2}}. \tag{22}$$

Substituting (22) into (21), the duty cycles D_1 and D_2 for Mode 2 can be determined.

3) Model 3: According to [37], the input current for Mode 3 is expressed as

$$|i_{pp}| = \frac{P_o}{v_{pn}} = \frac{v_oT_s}{8nL_r}2D_2\varphi_s. \tag{23}$$

Normalizing the input current, the input current in (23) can be rewritten in the following equation:

$$|y_{pp}| = 2D_2\varphi_s. \tag{24}$$

Then, the duty cycle expressions of Mode 3 in optimal TPS modulation can be solved by the KKT method

$$\begin{cases} D_2 = \frac{1}{M-1}\left(\frac{4nL_rI_{ZVS2}}{v_{pn}T_s} + \varphi_s\right) \\ D_1 = MD_2 + \frac{4L_rI_{ZVS1}}{v_{pn}T_s} \end{cases}. \tag{25}$$

Substituting (25) into (24), the phase shift angle is derived as follows:

$$\varphi_s = \sqrt{\left(\frac{2nL_rI_{ZVS2}}{v_{pn}T_s}\right)^2 + \frac{1}{2}(M-1)|y_{pp}|} - \frac{2nL_rI_{ZVS2}}{v_{pn}T_s}. \tag{26}$$

Substituting (26) into (25), the duty cycles D_1 and D_2 can be determined.

TABLE II
PHASE SHIFT ANGLES RANGE OF DIFFERENT OPTIMAL MODES

Working Mode		Range of φ_s
$M < 1$	Mode 1	$\varphi_s \in [0, \varphi_{b1}]$
where φ_{b1} = 1-M	Mode 2	$\varphi_s \in (\varphi_{b1}, 1]$
$M \geq 1$	Mode 3	$\varphi_s \in [0, \varphi_{b2}]$
where φ_{b2} = 1-1/M	Mode 4	$\varphi_s \in (\varphi_{b2}, 1]$

4) Model 4: According to [37], the input current of the DAB converter in Mode 4 can be expressed as follows:

$$|i_{pp}| = \frac{P_o}{v_{pn}} = \frac{v_oT_s}{8nL_r}\left(2\varphi_s - D_2^2 + 2D_2 - {\varphi_s}^2 - 1\right). \tag{27}$$

Similar to Mode 2, (27) can be reorganized as follows:

$$|y_{pp}| = 2\varphi_s - D_2^2 + 2D_2 - {\varphi_s}^2 - 1. \tag{28}$$

Then, the duty cycle expressions of Mode 4 in optimal TPS modulation can be solved by the KKT method

$$\begin{cases} D_2 = (2-M) + (M-1)\varphi_s \\ D_1 = 1 \end{cases}. \tag{29}$$

Substituting (29) into (28), the phase shift angle in Mode 4 can be derived as follows:

$$\varphi_s = 1 - \sqrt{\frac{1-|y_{pp}|}{M^2 - 2M + 2}}. \tag{30}$$

Substituting (30) into (29), the duty cycles D_1 and D_2 can be determined.

5) Boundary Conditions: As described above, when the conversion ratio $M < 1$, the DAB converter operates in Mode 1 under light load and Mode 2 under heavy load; when $M \geq 1$, it operates in Mode 3 under light load and Mode 4 under heavy load. According to the previous study [37], the phase shift angle ranges corresponding to each mode are summarized in Table II. φ_{b1} and φ_{b2} are the phase shift angle boundaries of Mode 1 & Mode 2 and Mode 3 & Mode 4, respectively.

B. Control Strategy and Modulation Scheme

In Section III-A, the different optimal working modes of the DAB converter are derived by analyzing the input current. In (16), (20), (24), and (28), y_{pp} is defined as normalized DAB input current, and its amplitude y can be used to regulate the output power. Due to the varied conversion ratio M with the input voltage v_{pn}, the working modes of the DAB converter must be switched within a cycle of input voltage to satisfy the specific load power. Therefore, in terms of the analysis in the previous section and the boundaries of different modes shown in Table II, the modulation scheme for the DAB converter is presented in Fig. 6. The conversion ratio M can be calculated through the sampled DAB input voltage v_{pn} and output voltage v_o. If $M < 1$, the DAB converter works in Mode 1 or Mode 2. Assuming it works in Mode 1, the phase shift angle $\varphi_{s\text{-}\mathrm{Mode1}}$ is calculated by (18). According to Table II, if $\varphi_{s\text{-}\mathrm{Mode1}} < \varphi_{b1}$, the converter works in Mode 1; if $\varphi_{s\text{-}\mathrm{Mode1}} \geq \varphi_{b1}$, the converter

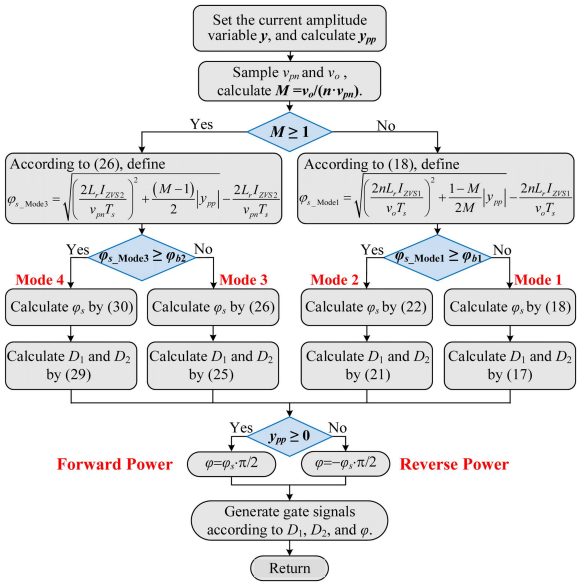

Fig. 6. Flowchart of the modulation scheme.

works in Mode 2. The corresponding duty cycles D_1 and D_2 are subsequently calculated from (17) for Mode 1 and (21) for Mode 2, respectively. Mode 3 and Mode 4 are selected by a similar procedure. Finally, if the normalized input current $y_{pp} > 0$, the converter operates in forward power flow with a positive phase shift angle; whereas it operates in reverse power flow with a negative phase shift angle. Therefore, the DAB input current can be directly controlled by adjusting the phase shift angle through the TPS modulation strategy, thereby achieving precise control of the ac input current.

The global control strategy of the system is illustrated in Fig. 7. The voltage-current closed-loop control is implemented to regulate the output voltage and control the current precisely. The voltage controller output y_v represents the normalized amplitude of the input current reference; the current controller output y is the normalized input current magnitude. As both controller outputs are dc values, PI controllers can be used to regulate the output voltage and the input current of the DAB converter. The controller design and implementation are greatly simplified. The grid phase angle θ from the phase-locked loop (PLL) is used to calculate the cosine values of the phase angles for the three-phase currents. The median among these cosine values is multiplied by y to generate the normalized third-harmonic injection current reference y_m*. Then, a conventional PI controller is used to control the third-harmonic injection current. The normalized input current y_{pp} of the DAB converter, calculated through (15), is also presented in this figure. Subsequently, D_1, D_2, and φ are derived from the DAB modulation scheme shown in Fig. 6. Finally, the gating signals are obtained.

C. Analyses of the Control Strategy

According to the modulation scheme and control strategy developed in Section III, the operating regions of different working modes of the DAB converter are shown in Fig. 8, where the grid line-to-line voltage is 200 V/50 Hz, output voltage $v_o = 200$ V or 250 V, turns ratio $n = 0.85$, series inductance $L_r = 36$ μH, $I_{ZVS1} = I_{ZVS2} = 1$ A, and switching period $T_s = 10$ μs. The symmetrical mode distributions for the bidirectional power flow are presented in one-third of a line frequency cycle. When $v_o = 200$ V, M is lower than 1. As shown in Fig. 8(a), the converter works in both Mode 1 and Mode 2 for $0 < y < 0.1787$. With the increase of y, it works exclusively in Mode 2. When $v_o = 250$ V, M is greater than 1. As shown in Fig. 8(b), the converter works in both Mode 3 and Mode 4 for $0 < y < 0.1682$. With the increase of y, it works exclusively in Mode 4.

Figs. 9 and 10 present the three-dimensional (3-D) modulation surfaces of D_1, D_2, φ_s, and y_{pp} as functions of the phase angle θ and y under different output voltage conditions. These surfaces cover all the required load power and conversion ratios. Complementing this, Fig. 11 illustrates the variation curves of D_1, D_2, and φ_s at discrete y values. When $v_o = 200$ V, if $y = 0.1$, the converter works in both Mode 1 and Mode 2; if $y = 0.8$, it works exclusively in Mode 2. When $v_o = 250$ V, if $y = 0.1$, the converter works in both Mode 3 and Mode 4; if $y = 0.8$, it works exclusively in Mode 4. Fig. 11 also demonstrates the range of working modes shown in Fig. 8.

IV. Optimization Design of the Magnetic Components

A. Third-Harmonic Injection Inductor Design

The design of the inductor L_m determines the third-harmonic injection current tracking accuracy, which directly influences the quality of the input current. The current flowing through L_m, which is denoted as i_m in Figs. 1 and 3, contains a ripple current. According to the operating principles mentioned in Section II, the ripple current in inductor L_m depends on the voltage across the inductor during the conduction of the switch S_{p1} and its conduction time. Therefore, the ripple current Δi_m is a function of the voltage phase θ. Taking sector I ($0 < \theta < \pi/3$) as an example, Δi_m can be expressed as follows:

$$\Delta i_m = \frac{v_{Lm}}{L_m} D_{p1} T_s = \frac{v_{ab} v_{bc}}{L_m f_s v_{ac}} = \frac{\sqrt{3} V_m}{L_m f_s} \frac{\cos(\theta + \pi/6)\sin(\theta)}{\cos(\theta - \pi/6)} \tag{31}$$

where v_{Lm} is the voltage across the inductor L_m, and f_s is the switching frequency. When $\theta = \pi/6$, the ripple current reaches the maximum value. The maximum ripple current $\Delta i_{m\_\max}$ is presented in the following equation:

$$\Delta i_{m\_\max} = \frac{\sqrt{3} V_m}{4 L_m f_s}. \tag{32}$$

Defining the ripple factor λ is the proportion of maximum ripple current to the amplitude of i_m (I_m/2). Thus, the inductance should satisfy the following equation:

$$L_m \geq \frac{\sqrt{3} V_m}{2\lambda I_m f_s}. \tag{33}$$

In this article, $\lambda = 0.22$ is adopted to balance the ripple suppression and volume of the inductor. According to the parameters shown in Table IV, the inductance should be larger than 984 μH. Finally, 1 mH is selected in the experiment.

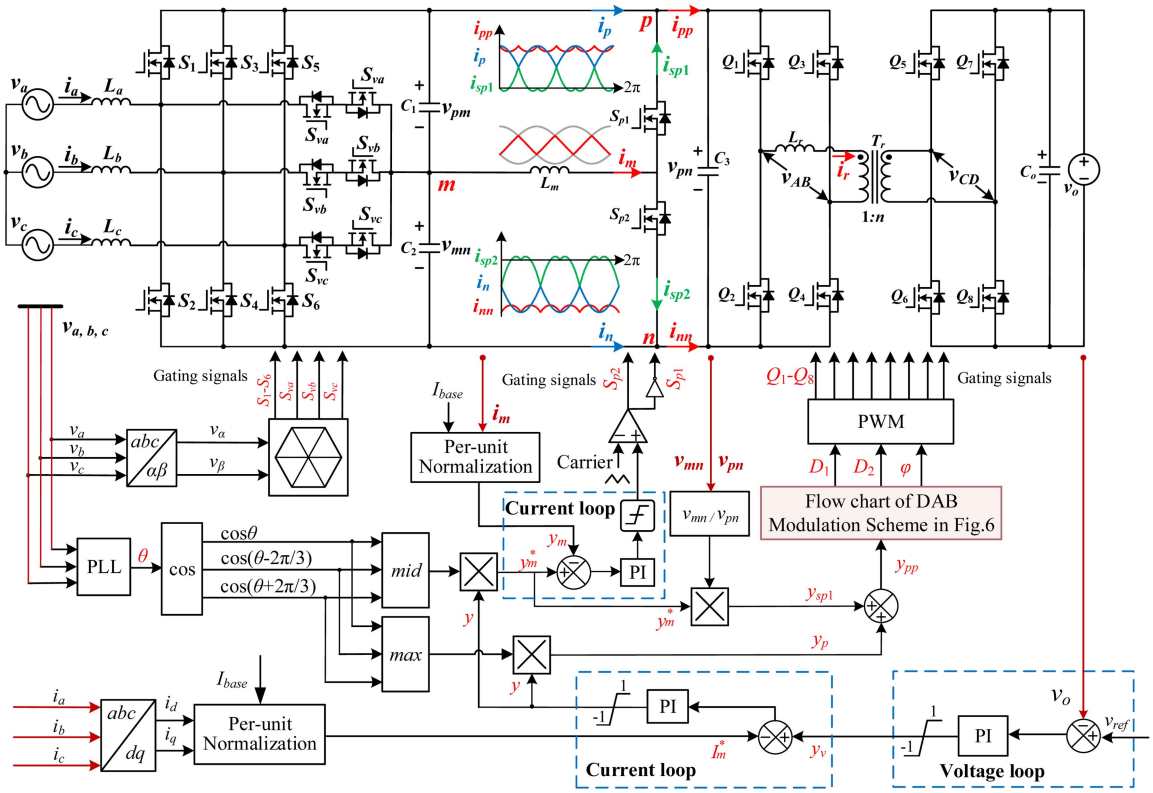

Fig. 7. Schematic diagram of the global control strategy.

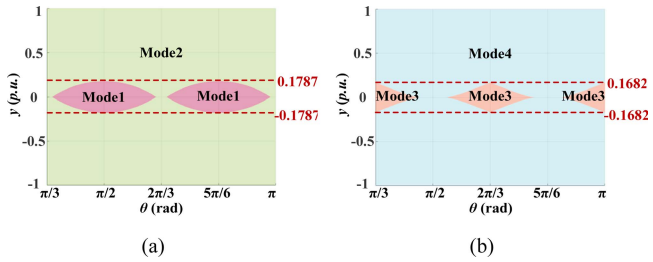

(a) (b)

Fig. 8. Distribution of working modes. (a) $v_o = 200$ V, $M < 1$. (b) $v_o = 250$ V, $M > 1$.

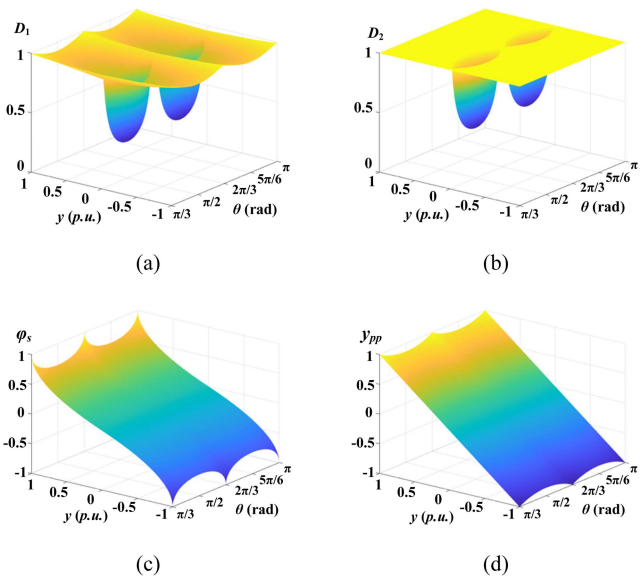

(a) (b) (c) (d)

Fig. 9. Three-dimensional modulation surfaces of D_1, D_2, φ_s, and y_{pp} versus the phase angle θ and y ($v_o = 200$ V, $M < 1$): (a) D_1 versus the phase angle θ and y; (b) D_2 versus the phase angle θ and y; (c) φ_s versus the phase angle θ and y; and (d) y_{pp} versus the phase angle θ and y.

B. Optimization Design of the Transformer and Series Inductor for DAB Converter Based on GA

As discussed in Section II-C, the switching loss of the low-frequency switches in IVS can be ignored, and the power loss of the H3R depends on the input current. However, for the DAB converter, the transformer turns ratio n and the series inductance L_r ultimately determine the operating modes and directly affect its efficiency. Furthermore, the series inductor current i_r is also closely related to n and L_r. Therefore, the total loss is related to n, L_r, and the working modes. To reduce losses and improve efficiency, coordinated optimization of n and L_r must be performed. However, the analytical expressions of the loss model are exceedingly complex, making it difficult to determine the optimal values of n and L_r through traditional analytical methods. Therefore, a numerical optimization method based on GA is proposed for optimal design of the transformer turns ratio n and the series inductance L_r. In this section, the total loss of

TABLE III
COMPARISON OF DIFFERENT THREE-PHASE SINGLE-STAGE AC–DC CONVERTERS

	[16]	[27]	[29]	This Work
Circuit topology	Three-phase matrix-type	SWISS+PSFB	SWISS+LLC	H3R+DAB
Bidirectional operation	Yes	No	No	Yes
Switching frequency	Constant frequency	Constant frequency	Variable frequency	Constant frequency
Soft switching	Not global soft switching	Not global soft switching	Not global soft switching	Global soft switching
Number of transformers	1	2	1	1
Number of energy storge components	1*L*	3*L*	2*L*+1*C*	2*L*
Number of switches and diodes	16 switches	14 switches+10 diodes	14 switches+10 diodes	22 switches
Power density	High	Low	Low	Moderate
Complexity	High	Moderate	Moderate	Low
Efficiency	Low	Moderate	Moderate	High
Peak efficiency	90.4%	95%	96.2%	97.6%
Modulation scheme	TZM	PWM	PFM+PWM	TPS

Notation:
L: Energy storage inductor; *C*: Energy storage capacitor

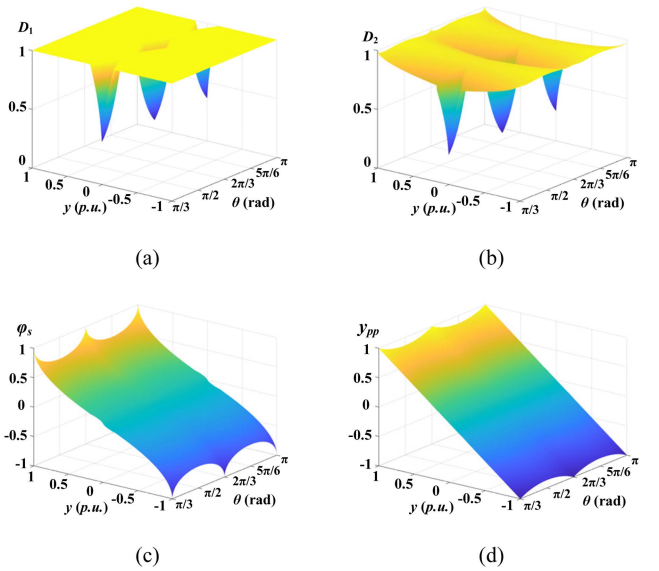

Fig. 10. Three-dimensional modulation surfaces of D_1, D_2, φ_s, and y_{pp} versus the phase angle θ and y (v_o= 250 V, $M > 1$): (a) D_1 versus the phase angle θ and y; (b) D_2 versus the phase angle $\theta$and y; (c) φ_s versus the phase angle θ and y; and (d) y_{pp} versus the phase angle θ and y.

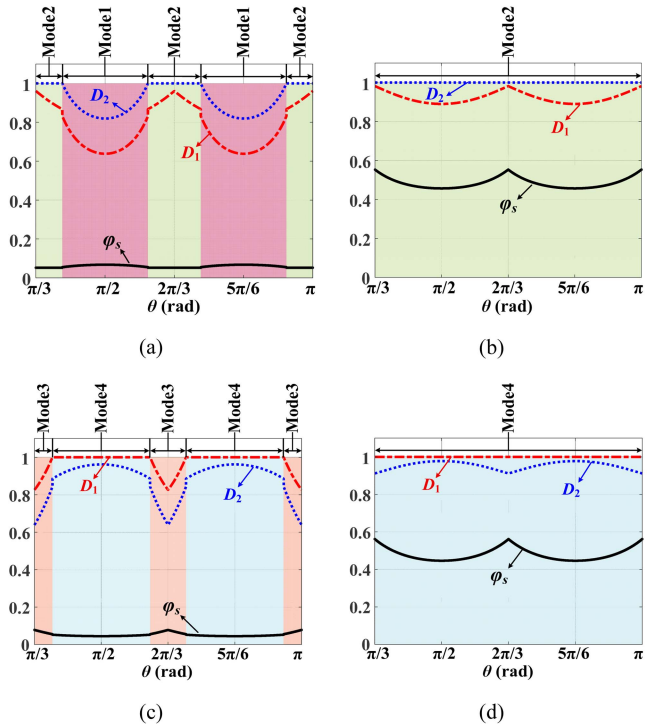

Fig. 11. Curves of D_1, D_2, and φ_s versus the phase angle θ for different y. v_o = 200 V. (a) $y = 0.1$. (b) $y = 0.8$; $v_o = 250$ V. (c) $y = 0.1$. (d) $y = 0.8$.

the DAB converter is minimized as the optimization objective function to obtain the optimal parameters. Furthermore, the modulation scheme proposed for the DAB converter can achieve ZVS. Therefore, the switching loss only includes the turn-OFF loss of the switches in the DAB converter.

According our previous study [34], [38], the total loss of the DAB converter $P_{\mathrm{DAB\cdot loss}}$ is expressed as follows:

$$P_{\mathrm{DAB\_loss}} = P_{\mathrm{DAB\_}c} + P_{\mathrm{DAB\_off}} + P_{\mathrm{core}} + P_{\mathrm{copper}} \quad (34)$$

where $P_{\mathrm{DAB\cdot}c}$ is the conduction loss of the switches in the DAB converter, $P_{\mathrm{DAB\cdot off}}$ is the turn-OFF loss, P_{core} and P_{copper} represent the core loss and copper loss of the transformer and series inductor, respectively. More detailed derivations can be referred to the previous study in [34], [38].

TABLE IV
DETAILED SPECIFICATIONS

Items	Symbol	Parameter
RMS line-to-line AC voltage	v_{AB}, v_{BC}, v_{CA}	200 V/50 Hz
Output voltage	v_o	200 V/250 V
Turns ratio of the transformer	n	0.85 (PQ40/40)
Switching frequency (period)	f_s (T_s)	100 *k*Hz(10 μs)
Switches	$S_{1\text{-}6}$, $S_{va\text{-}vc}$ $S_{p1\text{-}p2}$, $Q_{1\text{-}8}$	C3M0065090D
series inductor	L_r	36 μH (PQ32/30)
Input filter inductor	L_a, L_b, L_c	22 μH
Input filter capacitance	C_1, C_2	2 μF
	C_3	3.3 μF
Output filter capacitance	C_o	1090 μF

The conduction loss of the H3R includes the losses in the three-phase full-bridge $P_{\text{bridge}\cdot c}$, bidirectional switches $P_{bs\cdot c}$, and Y-bridge arm $P_{Y\cdot c}$. Therefore, the total conduction loss in H3R is given by the following equation:

$$P_{\text{H3R\_}c} = P_{\text{bridge\_}c} + P_{bs\_c} + P_{Y\_c} = \left(i^2_{\text{bridge\_rms}} + i^2_{bs\_\text{rms}} + i^2_{Y\_\text{rms}}\right) \cdot 2R_{\text{ds(on)}} \tag{35}$$

where $R_{\text{ds(on)}}$ is the on-resistance of the switches, $i_{\text{bridge}\cdot\text{rms}}$ is the RMS current flowing through the three-phase full-bridge switches, $i_{bs\cdot\text{rms}}$ and $i_{Y\cdot\text{rms}}$ are the RMS current through the bidirectional switches and the switch S_{p1}, respectively.

In the H3R topology, the switching loss is solely contributed by the switches S_{p1} and S_{p2} in the Y-bridge arm. Similar to the DAB loss calculation method, the switching loss of H3R $P_{\text{H3R}\cdot sw}$ is expressed as follows:

$$P_{\text{H3R\_sw}} = P_{\text{H3R\_off}} + P_{\text{H3R\_on}} = \frac{1}{\pi}\int_0^{\pi} 2P_{\text{off\_sp1}}d\theta + \frac{1}{\pi}\int_0^{\pi} 2P_{\text{on\_sp1}}d\theta \tag{36}$$

where $P_{\text{H3R}\cdot\text{off}}$ and $P_{\text{H3R}\cdot\text{on}}$ are the turn-OFF loss and turn-ON loss of the H3R, $P_{\text{off}\cdot\text{sp1}}$ and $P_{\text{on}\cdot\text{sp1}}$ are the turn-OFF loss and turn-ON loss of the switch S_{p1}.

Since the third-harmonic injection inductor L_m operates at a low frequency, the core loss can be ignored. Thus, the copper loss of the inductor $P_{Lm\cdot\text{loss}}$ is calculated as

$$P_{\text{Lm\_loss}} = i^2_{m\_\text{rms}} \cdot R_{\text{dc}} \tag{37}$$

where $i_{m\cdot\text{rms}}$ is the rms value of the third-harmonic current i_m, R_{dc} is the dc resistance of the inductor.

Moreover, according to (13), (19), (23), and (27), when $D_1 = 1$, $D_2 = 1$, and $\varphi_s = 1$, the amplitude of the input current i_{pp} reaches the maximum value $I_{\max}$, which is expressed in the following equation:

$$I_{\max} = \frac{V_o T_s}{8nL_r}. \tag{38}$$

For the DAB converter, the input voltage and current in a sector ($\pi/3 < \theta < 2\pi/3$) can be expressed as follows:

$$\begin{cases} v_{pn} = v_{bc} = \sqrt{3}V_m \cos(\theta - \frac{\pi}{2}) \\ i_{pp} = i_p + i_m\frac{v_{mn}}{v_{pn}} = i_b + i_a\frac{v_{mn}}{v_{pn}} = i_b + i_a\frac{v_{ac}}{v_{bc}} \\ = I_{max}\cos(\theta - \frac{2\pi}{3}) + I_{max}\cos(\theta)\frac{\cos(\theta-\frac{\pi}{6})}{\cos(\theta-\frac{\pi}{2})} \end{cases}. \tag{39}$$

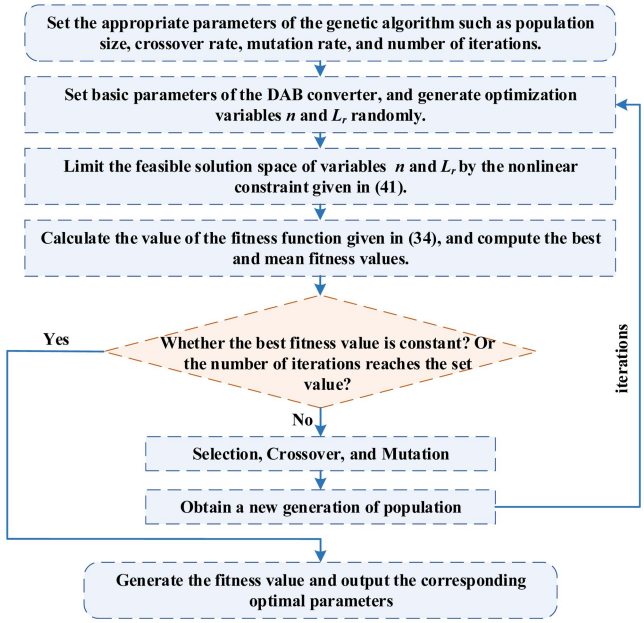

Fig. 12. Flowchart of GA-based parameters design for the transformer and series inductor.

Therefore, the maximum input power $P_{in\cdot\max}$ is presented in the following equation:

$$P_{in\_max} = \frac{3}{\pi}\int_{\pi/3}^{2\pi/3} v_{pn}i_{pp}d\theta = \frac{3v_oV_mT_s}{16nL_r}. \tag{40}$$

The maximum input power $P_{in\cdot\max}$ must be greater than the maximum output power requirement $P_{o\cdot\max}$

$$P_{in\_\max} = \frac{3v_oV_mT_s}{16nL_r} \geq P_{o\_\max} \Rightarrow nL_r \leq \frac{3v_oV_mT_s}{16P_{o\_\max}}. \tag{41}$$

Based on the loss analysis above, the total loss of the DAB converter $P_{\text{DAB}\cdot\text{loss}}$ given in (34) is the fitness function to determine the optimal parameters. The output power requirement expressed in (41) is set as the constraint. According to our previous study [38], the transformer core and inductor core are selected by the AP value. The PQ core series is adopted as the candidate magnetic core. The AP value and total loss are functions of the selected turns ratio n and series inductance L_r. Thus, n and L_r are optimization variables whose initial values are randomly generated within a defined range. The flowchart of the parameters of the transformer and series inductor design based on GA is shown in Fig. 12.

Under the following conditions: input line-to-line voltage is 200 V/50 Hz, output voltage $v_o = 200$ V, switching frequency $f_s = 100$ kHz, the maximum output power $P_{o\cdot\max} = 2$ kW, and the rated output power is 1.6 kW. In terms of the created libraries for commercially available cores and litz wires, the minimum total loss of the DAB converter is determined via a traditional GA. As shown in Fig. 13, the best and mean fitness values per

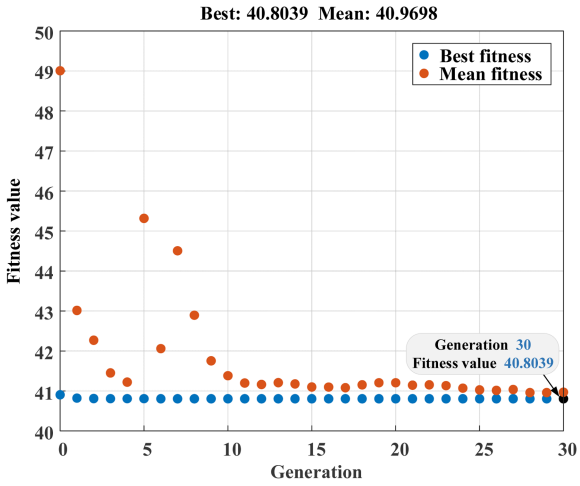

Fig. 13. Variation of the DAB total loss with the iteration number.

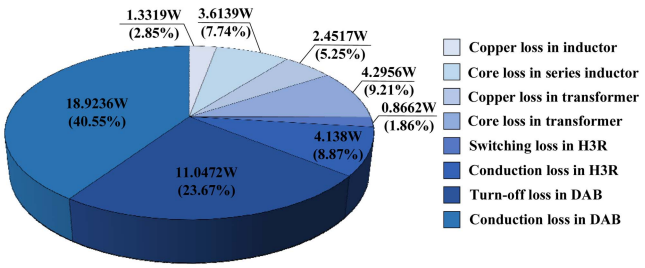

Fig. 14. Loss distribution for 1600 W load power.

generation are plotted, and the best fitness converges within 15 generations.

The minimum total loss of the DAB converter is 40.8 W, shown in Fig. 13. The corresponding optimal parameters of the final solution are given in below: the turns ratio $n = 0.85$, the series inductance $L_r = 36$ μH, the cores selected for the transformer and series inductor are PQ40/40 and PQ32/30, respectively.

For the proposed GA-based optimization method, the maximum generation count and population size per generation are set to 30 and 100, respectively. Thus, the computational count is only 3000 (100·30). In contrast, the parameter enumeration method explores all design possibilities by freely varying each parameter. The feasible solution space of the transformer turns ratio n is defined as [0.1, 2]. According to the nonlinear constraints given in (41), the range of the series inductance L_r is set to [10 μH, 306 μH]. With step sizes of 0.01 for n and 1 μH for L_r, the computational count reaches 56727 (191·297) using the parameter enumeration approach. Therefore, the number of evaluations of the proposed optimization method is significantly lower than that of the parameter enumeration method, demonstrating its greater practicality for engineering implementation.

To further analyze the loss model, the loss distribution of the three-phase ac–dc converter under 200 V output voltage and 1600 W rated power is shown in Fig. 14. It can be observed that the conduction loss of the switching devices constitutes the largest proportion of the total converter losses, accounting for approximately 49.42%, followed by the turn-OFF loss of the switches in the DAB converter, about 23.67%. In addition, the switching loss of the switches S_{p1} and S_{p2} in H3R is only 0.8662 W (1.86%).

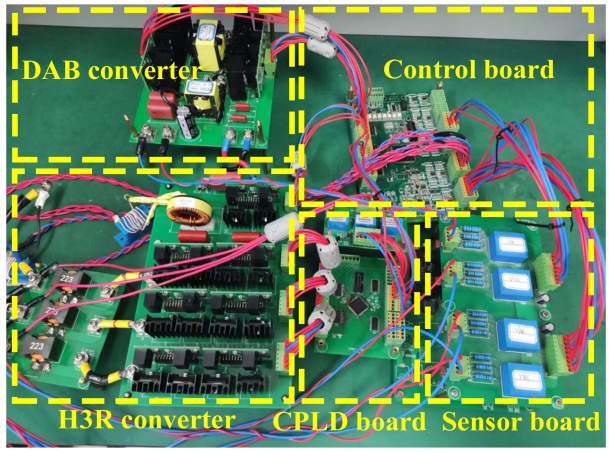

Fig. 15. Experimental prototype for test.

Table III presents the comprehensive comparison of the different three-phase single-stage isolated ac–dc converters. The three-phase single-stage isolated matrix-type converter in [16] uses the fewest switching devices and achieves high power density. Compared to the other three-phase single-stage ac–dc topologies in [27] and [29], the proposed converter utilizes fewer switching devices and energy storage components, thereby reducing the design and control complexity, while improving efficiency and power density. In [16], the complex dual-period-decoupled space vector TZM technique fails to account for the switching losses. As most switches operate in hard switching, the converter exhibits significant switching losses, resulting in lower efficiency. The up-counting mode-based pulsewidth modulation (PWM) is proposed in [27] to achieve ZVS for the lagging switches. However, this method results in substantially complicated operating modes and fails to ensure global soft switching. To further extend the soft switching range, the hybrid pulse frequency modulation and pulse width modulation (PFM+PWM) scheme is developed in [29], though this increases the design and control complexity. Furthermore, both solutions in [27] and [29] are suitable only for unidirectional power flow. The proposed control strategy and modulation scheme achieve wide-range soft-switching operation across diverse operating conditions, thus reducing the power loss and improving energy conversion efficiency. Overall, the proposed topology demonstrates superior performance for single-stage isolated bidirectional ac–dc power conversion, outperforming other approaches in power density, efficiency, and control simplicity.

V. Experimental Verification

A 1.6-kW experimental prototype operating at 200 V/50 Hz, as shown in Fig. 15, is built to validate the control strategy and modulation scheme. Table IV lists all detailed

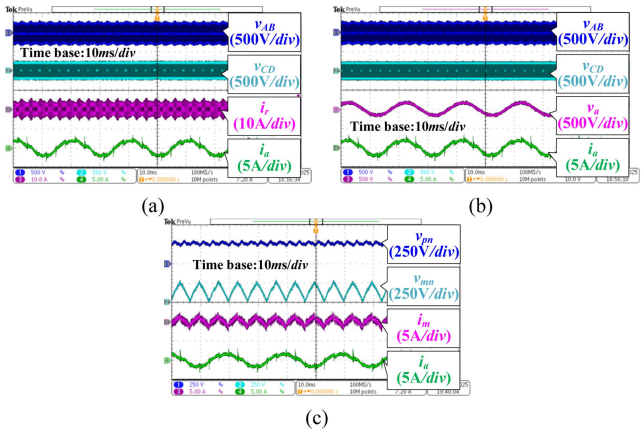

Fig. 16. Steady-state experimental waveforms at 200 V output voltage and 500 W load. (a) Full bridge voltages v_{AB}, v_{CD}, and series inductor current i_r. (b) Phase voltage v_a and phase current i_a. (c) Output voltage of the H3R v_{pn} and third-harmonic injection current i_m.

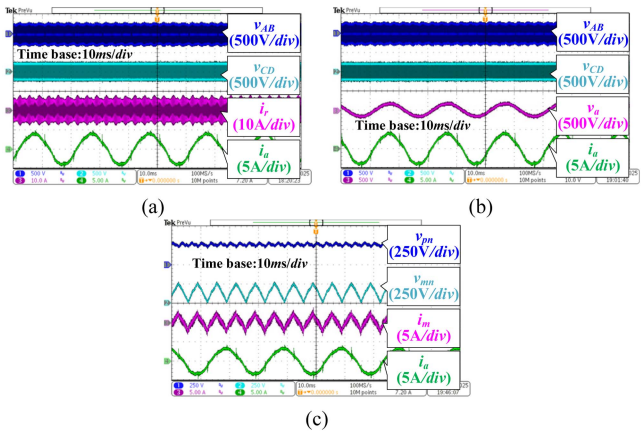

Fig. 17. Steady-state experimental waveforms at 200 V output voltage and 1000 W load. (a) Full bridge voltages v_{AB}, v_{CD}, and series inductor current i_r. (b) Phase voltage v_a and phase current i_a. (c) Output voltage of the H3R v_{pn} and third-harmonic injection current i_m.

parameters of the converter. The control strategy and modulation scheme are implemented in a TMS320F28377 DSP, while the EPM240T100C5N CPLD generates gate signals for the IVS.

Figs. 16 –18 show the steady-state waveforms of the converter operating at $v_o = 200$ V under 500 W, 1 kW, and 1.6 kW load power. It can be observed that the envelope curve of v_{AB} correlates with the DAB input voltage v_{pn}. Figs. 16(b)–18(b) present the phase voltage is in phase with the phase current. These synchronized waveforms indicate that the unit PF can be achieved under different power levels. Figs. 16(c)–18(c) mainly display the output voltage of the H3R v_{pn}, which is a sixfold line-frequency fluctuating dc voltage, and third-harmonic injection current i_m. These current waveforms demonstrate that the third-harmonic injection current i_m and input phase current can be precisely controlled by the proposed voltage-current closed-loop cooperative control strategy at different power levels.

Figs. 19 –21 display the experimental waveforms of the DAB converter at 500 W, 1 kW, and 1.6 kW load power with different

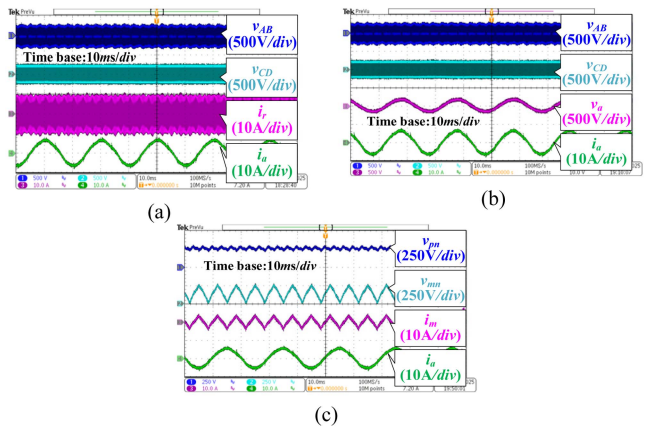

Fig. 18. Steady-state experimental waveforms at 200 V output voltage and 1600 W load. (a) Full bridge voltages v_{AB}, v_{CD}, and series inductor current i_r. (b) Phase voltage v_a and phase current i_a. (c) Output voltage of the H3R v_{pn} and third-harmonic injection current i_m.

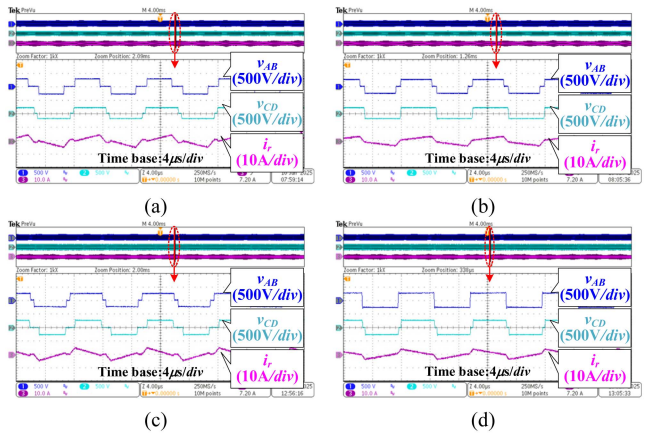

Fig. 19. Key waveforms of the DAB converter at 500 W load. (a) Mode 1 ($v_o = 200$ V, $M < 1$). (b) Mode 2 ($v_o = 200$ V, $M < 1$). (c) Mode 3 ($v_o = 250$ V, $M > 1$). (d) Mode 4 ($v_o = 250$ V, $M > 1$).

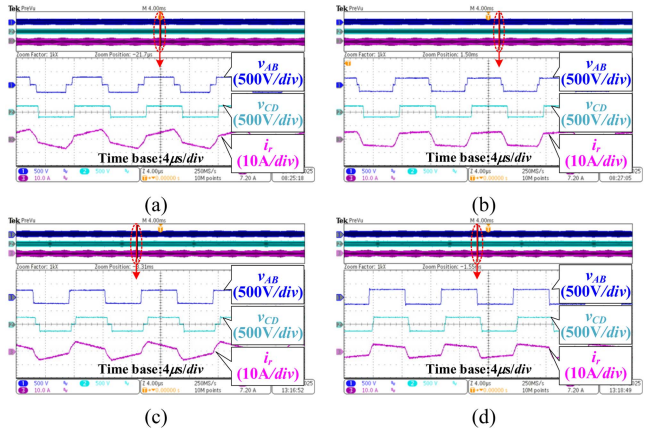

Fig. 20. Key waveforms of the DAB converter at 1000 W load. (a) Mode 2 ($v_o = 200$ V, v_{pn} at maximum voltage). (b) Mode 2 ($v_o = 200$ V, v_{pn} at minimum voltage). (c) Mode 4 ($v_o = 250$ V, v_{pn} at minimum voltage). (d) Mode 4 ($v_o = 250$ V, v_{pn} at maximum voltage).

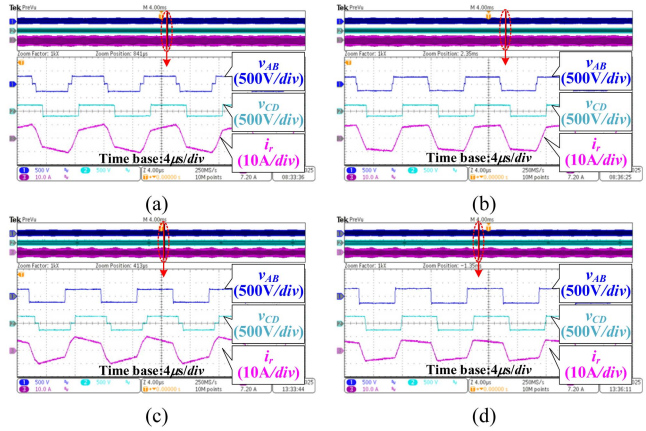

Fig. 21. Key waveforms of the DAB converter at 1600 W load. (a) Mode 2 (v_o = 200 V, v_{pn} at maximum voltage). (b) Mode 2 (v_o = 200 V, v_{pn} at minimum voltage). (c) Mode 4 (v_o = 250 V, v_{pn} at minimum voltage). (d) Mode 4 (v_o = 250 V, v_{pn} at maximum voltage).

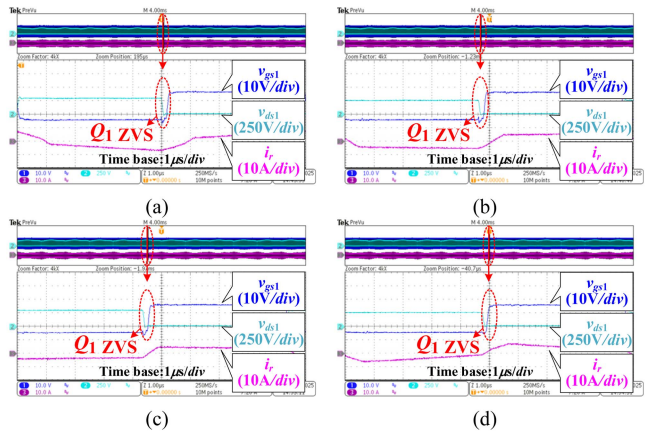

Fig. 22. Gate signal and drain-source voltage of switch Q_1 at 1000 W load. (a) Mode 2 (v_o = 200 V, v_{pn} at maximum voltage). (b) Mode 2 (v_o = 200 V, v_{pn} at minimum voltage). (c) Mode 4 (v_o = 250 V, v_{pn} at maximum voltage). (d) Mode 4 (v_o = 250 V, v_{pn} at minimum voltage).

output voltages, respectively. The key waveforms illustrated in Fig. 5 are validated experimentally in Fig. 19 at 500 W load power. Figs. 20 and 21 demonstrate that the DAB converter only works in Mode 2 and Mode 4 with increasing power, which is consistent with the theoretical analysis in Fig. 8.

Figs. 22 –25 show the gate signals and drain-source voltages of the switches in the DAB converter at 1000 W load. It is clear that ZVS is achieved as the drain-source voltage reaches zero before the corresponding switches turn ON. The other switches in the same bridge exhibit similar ZVS performance, demonstrating that the proposed globally optimized TPS modulation scheme can enable ZVS for all switches in the DAB converter.

Figs. 26 and 27 show the dynamic response of the load step change from 500 to 1300 W and from 1300 to 500 W, respectively. These results verify the satisfactory dynamic performance during both upward and downward load transitions. The input

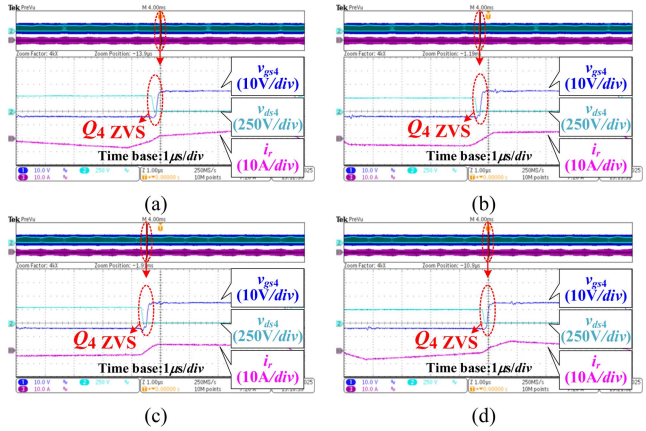

Fig. 23. Gate signal and drain-source voltage of switch Q_4 at 1000 W load. (a) Mode 2 (v_o = 200 V, v_{pn} at maximum voltage). (b) Mode 2 (v_o = 200 V, v_{pn} at minimum voltage). (c) Mode 4 (v_o = 250 V, v_{pn} at maximum voltage). (d) Mode 4 (v_o = 250 V, v_{pn} at minimum voltage).

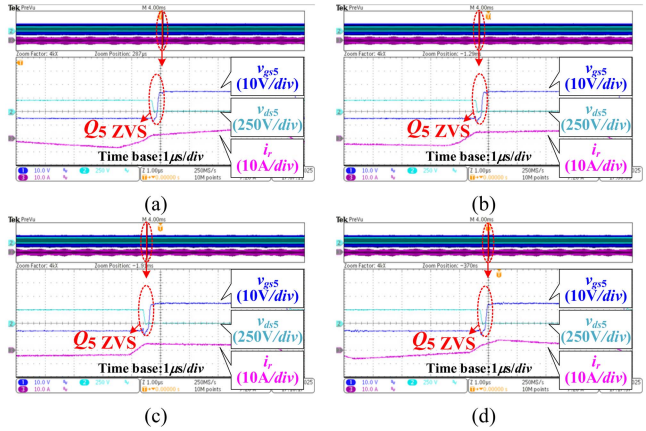

Fig. 24. Gate signal and drain-source voltage of switch Q_5 at 1000 W load. (a) Mode 2 (v_o = 200 V, v_{pn} at maximum voltage). (b) Mode 2 (v_o = 200 V, v_{pn} at minimum voltage). (c) Mode 4 (v_o = 250 V, v_{pn} at maximum voltage). (d) Mode 4 (v_o = 250 V, v_{pn} at minimum voltage).

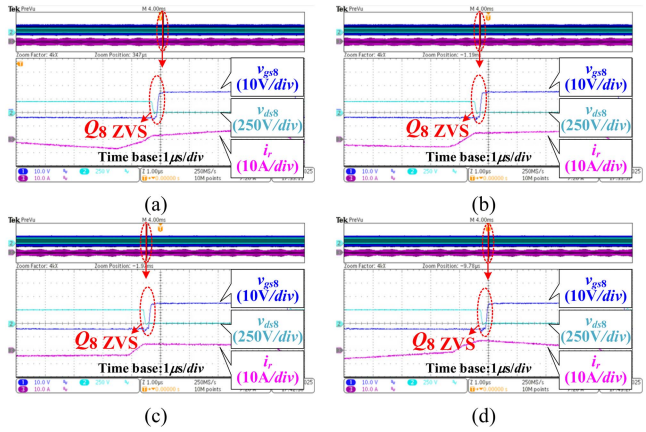

Fig. 25. Gate signal and drain-source voltage of switch Q_8 at 1000 W load. (a) Mode 2 (v_o = 200 V, v_{pn} at maximum voltage). (b) Mode 2 (v_o = 200 V, v_{pn} at minimum voltage). (c) Mode 4 (v_o = 250 V, v_{pn} at maximum voltage). (d) Mode 4 (v_o = 250 V, v_{pn} at minimum voltage).

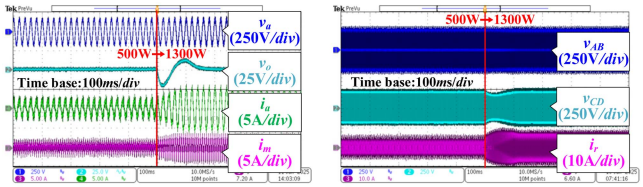

(a) (b)

Fig. 26. Dynamic response under 200 V output voltage and the load step change from 500 to 1300 W. (a) Output voltage v_o, phase current i_a, and third-harmonic injection current i_m. (b) Full bridge voltages v_{AB}, v_{CD}, and series inductor current i_r.

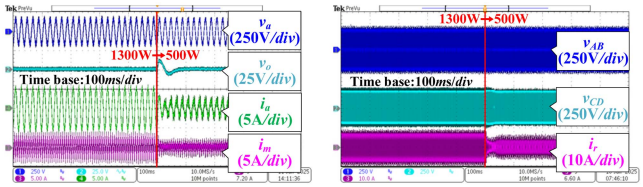

(a) (b)

Fig. 27. Dynamic response under 200 V output voltage and the load step change from 1300 to 500 W. (a) Output voltage v_o, phase current i_a, and third-harmonic injection current i_m. (b) Full bridge voltages v_{AB}, v_{CD}, and series inductor current i_r.

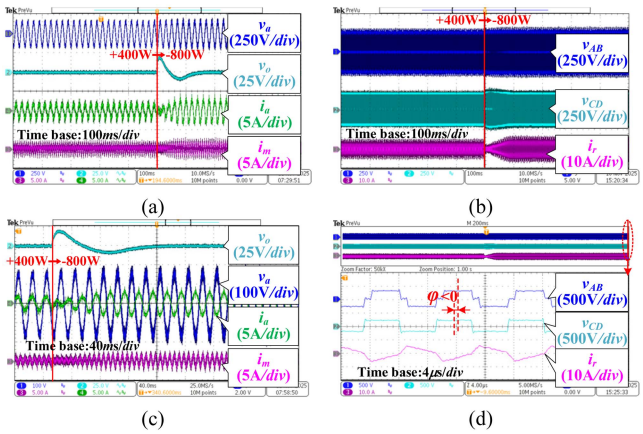

(a) (b) (c) (d)

Fig. 28. Dynamic response under 200 V output voltage and the load step change from forward 400 to reverse 800 W. (a) Phase voltage v_a, output voltage v_o, phase current i_a, and third-harmonic injection current i_m. (b) Full bridge voltages v_{AB}, v_{CD}, and inductor current i_r. (c) Zoomed-in waveforms of Fig. 28(a). (d) Zoomed-in waveforms (Mode 2) in reverse power flow.

phase current and series inductor current exhibit smooth transitions without oscillation. These waveforms confirm the excellent dynamic response of the proposed control strategy.

Fig. 28 presents the waveforms in the reverse power flow. The dynamic response of the load step change from forward 400 to reverse 800 W is shown in Fig. 28(a) and (b). As shown in Fig. 28(c), the phase current is in phase with the phase voltage at forward 400 W. At reverse 800 W, it exhibits a 180° phase shift, indicating that the converter is operating in the reverse power flow. The key waveforms of the DAB converter in reverse power flow with a negative phase shift angle are presented in

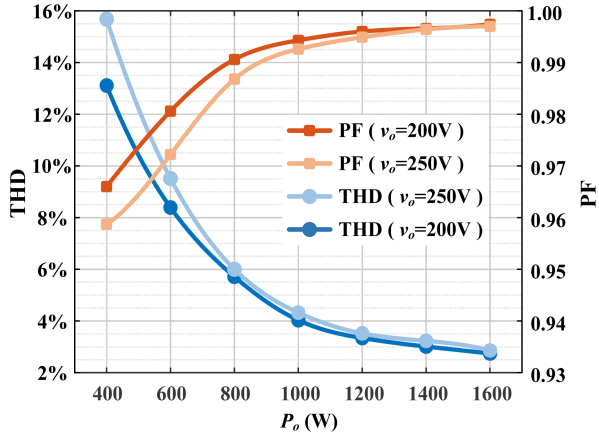

Fig. 29. PF and THD of the grid current at different output voltages.

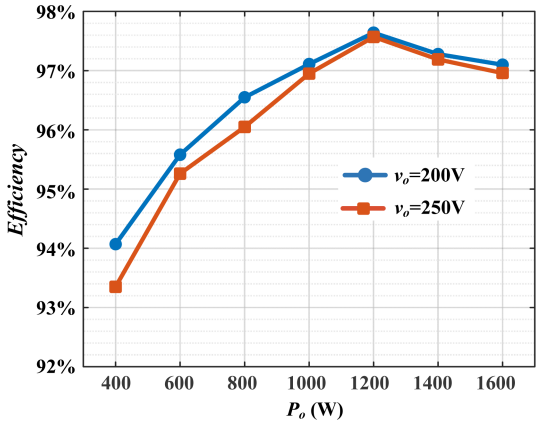

Fig. 30. Measured efficiency versus output power at different output voltages.

Fig. 28(d), which are symmetric to the forward power flow waveforms discussed in Section III.

Fig. 29 presents total harmonic distortion (THD) and PF versus output power. These results indicate that the THD decreases and PF improves with increasing load power. In addition, at 200 V output voltage, both THD and PF exhibit better performance compared to those at 250 V output voltage. At 200 V output voltage and rated 1600 W load power, the THD is 2.74% and the PF achieves 0.997. It demonstrates that the proposed control strategy achieves high PF and low THD across the wide load range.

To verify the prototype efficiency and the accuracy of the loss model, the measured efficiency of the converter is shown in Fig. 30. It can be observed that the efficiency at 200 V output voltage is slightly higher than that at 250 V. Under 200 V operation, the peak efficiency reaches 97.6% at 1200 W load, while still remaining 97.1% at the rated 1600 W load. Fig. 31 shows the thermal performance of the DAB-based ac–dc converter operating at the full load of 1600 W. As shown in Fig. 31(a), the maximum temperature recorded was approximately 37 °C after 5 min of operation. The highest temperature regions are primarily concentrated in the DAB converter, particularly in the

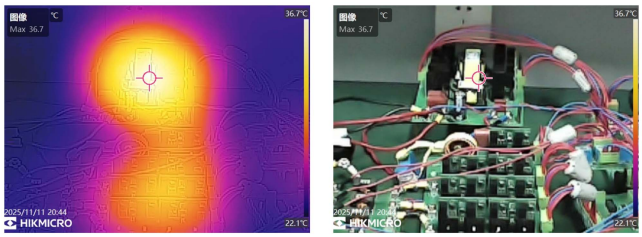

(a) (b)

Fig. 31. Thermal and visible light images of the AC–DC converter operating at 1600 W load power. (a) Thermal image. (b) Visible light image.

transformer. This indicates that the power losses are mainly concentrated in these components. Both the measured efficiency and the thermal image closely match the model-based loss analysis shown in Fig. 14. The high conversion efficiency demonstrates the effectiveness of the GA-based optimization method for the magnetic component parameters.

VI. Conclusion

This article proposes a higher-efficiency three-phase quasi-single-stage isolated bidirectional ac–dc converter. By analyzing the input current of the DAB converter, the optimal working modes and the modulation scheme are developed to realize the wide-range ZVS operation. The proposed voltage-current closed-loop control strategy regulates the output voltage while precisely controlling the third-harmonic current to achieve sinusoidal input phase current, ensuring the unity PF with low THD. The operating regions of different working modes and the variation patterns of control variables are analyzed in detail under varying load and phase angle conditions. Moreover, to further improve the efficiency, the magnetics of the DAB converter are optimized using GA to minimize total loss. Experimental results demonstrate that the proposed DAB-based H3R ac–dc converter achieves 97.6% peak efficiency. At rated load, it maintains 97.1% efficiency with 2.74% input current THD. The demonstrated superior performance indicates that the proposed solution is an attractive candidate for bidirectional ac–dc power conversion systems.

References

[1] A. Ivanovsky, V. Y. Frolov, and D. V. Ivanov, "Development of a three-phase AC/DC converter for charging batteries including electric vehicles," in *Proc. Seminar Elect. Eng., Autom. Control Syst., Theory Practical Appl.*, 2023, pp. 136–139.

[2] F. Wu, K. Wang, G. Hu, Y. Shen, and S. Luo, "Overview of single-stage high-frequency isolated AC–DC converters and modulation strategies," *IEEE Trans. Power Electron.*, vol. 38, no. 2, pp. 1583–1598, Feb. 2023.

[3] P. Nayak and K. Rajashekara, "A single-stage isolated AC–DC converter to interlink utility grid and renewable energy sources in a residential DC distribution system," *IEEE Trans. Ind. Appl.*, vol. 57, no. 5, pp. 4409–4419, Sep./Oct. 2021.

[4] M. Safayatullah, M. T. Elrais, S. Ghosh, R. Rezaii, and I. Batarseh, "A comprehensive review of power converter topologies and control methods for electric vehicle fast charging applications," *IEEE Access*, vol. 10, pp. 40753–40793, 2022.

[5] H. Wang and F. Blaabjerg, "Reliability of capacitors for DC-link applications in power electronic converters—An overview," *IEEE Trans. Ind. Appl.*, vol. 50, no. 5, pp. 3569–3578, Sep./Oct. 2014.

[6] R. Baranwal, K. V. Iyer, K. Basu, G. F. Castelino, and N. Mohan, "A reduced switch count single-stage three-phase bidirectional rectifier with high-frequency isolation," *IEEE Trans. Power Electron.*, vol. 33, no. 11, pp. 9520–9541, Nov. 2018.

[7] E. L. Carvalho, A. Blinov, A. Chub, and D. Vinnikov, "Overview of single-stage isolated AC-DC topologies for interfacing DC and AC grids," in *Proc. IEEE 13th Int. Symp. Power Electron. Distrib. Gener. Syst.*, 2022, pp. 1–6.

[8] Y. Xu, Z. Wang, Y. Shen, Z. Zou, and M. Liserre, "A VSC-based isolated matrix-type AC/DC converter without bidirectional power switches," *IEEE Trans. Ind. Electron.*, vol. 70, no. 12, pp. 12442–12452, Dec. 2023.

[9] H. Kim, H. Belkamel, J. Park, R. M. Hakim, and S. Choi, "Modular three-phase single-stage isolated AC-DC converter for electrolytic capacitor-less EV DC charging," in *Proc. IEEE 9th Int. Power Electron. Motion Control Conf.*, 2020, pp. 1573–1578.

[10] L. Schrittwieser, P. Cortés, L. Fässler, D. Bortis, and J. W. Kolar, "Modulation and control of a three-phase phase-modular isolated matrix-type PFC rectifier," *IEEE Trans. Power Electron.*, vol. 33, no. 6, pp. 4703–4715, Jun. 2018.

[11] W. Hu, Y. Xie, Z. Wang, Z. Zhang, and Y. Guan, "A Family of asymmetrical SVPWM schemes with normal and open-circuit fault-tolerant operation capability for a three-phase isolated AC–DC matrix converter," *IEEE Trans. Power Electron.*, vol. 37, no. 2, pp. 1788–1803, Feb. 2022.

[12] W. Hu, Y. Xie, Y. Guan, Z. Wang, and Z. Zhang, "Quasi-symmetrical SVPWM scheme based on general volt-second balance model for a three-phase isolated AC–DC matrix converter," *IEEE Trans. Power Electron.*, vol. 38, no. 10, pp. 12704–12718, Oct. 2023.

[13] F. Fang, H. Tian, and Y. Li, "Coordination control of modulation index and phase shift angle for current stress reduction in isolated AC–DC matrix converter," *IEEE Trans. Power Electron.*, vol. 36, no. 4, pp. 4585–4596, Apr. 2021.

[14] X. Guo, L. Zhang, Y. Wei, and S. Wu, "A coordination control method for current stress reduction in high-frequency link matrix converter," *IEEE Trans. Ind. Electron.*, vol. 71, no. 9, pp. 9972–9981, Sep. 2024.

[15] X. Li, F. Wu, G. Yang, H. Liu, and T. Meng, "Dual-period-decoupled space vector phase-shifted modulation for DAB-based three-phase single-stage AC–DC converter," *IEEE Trans. Power Electron.*, vol. 35, no. 6, pp. 6447–6457, Jun. 2020.

[16] F. Wu, X. Li, G. Yang, H. Liu, and T. Meng, "Variable switching periods based space vector phase-shifted modulation for DAB based three-phase single-stage isolated AC–DC converter," *IEEE Trans. Power Electron.*, vol. 35, no. 12, pp. 13725–13734, Dec. 2020.

[17] Z. Guo, Z. Wang, L. Liu, and Z. Chen, "Efficiency-optimization control strategy with real-time modulation scheme for three-phase single-stage matrix-type isolated AC-DC converters," *IEEE Trans. Power Electron.*, vol. 41, no. 3, pp. 4087–4103, Mar. 2026, doi: 10.1109/TPEL.2025.3616208.

[18] Z. Guo, W. Zhan, and Z. Chen, "Control Strategy of three-phase single-stage matrix-type isolated AC-DC converters with three-order resonant tank," *IEEE Trans. Power Electron.*, vol. 41, no. 3, pp. 4057–4071, Mar. 2026, doi: 10.1109/TPEL.2025.3613728.

[19] D. Das, N. Weise, K. Basu, R. Baranwal, and N. Mohan, "A bidirectional soft-switched DAB-based single-stage three-phase AC–DC converter for V2G application," *IEEE Trans. Transp. Electrific.*, vol. 5, no. 1, pp. 186–199, Mar. 2019.

[20] L. Schrittwieser, M. Leibl, and J. W. Kolar, "99% Efficient isolated three-phase matrix-type DAB buck–boost PFC rectifier," *IEEE Trans. Power Electron.*, vol. 35, no. 1, pp. 138–157, Jan. 2020.

[21] N. B. Y. Gorla, J. Saha, K. Jayraman, and S. K. Panda, "A modulation strategy with transformer leakage inductance energy management for a three-phase matrix-based isolated AC–DC converter," *IEEE J. Emerg. Sel. Topics Power Electron.*, vol. 11, no. 3, pp. 2780–2792, Jun. 2023.

[22] J. Saha, R. K. Singh, and S. K. Panda, "Three-phase matrix-based isolated AC-DC converter for battery energy storage system," in *Proc. IEEE 12th Int. Symp. Power Electron. Distrib. Gener. Syst.*, 2021, pp. 1–8.

[23] F. Fang, H. Tian, and Y. Li, "SVM strategy for mitigating low-order harmonics in isolated AC–DC matrix converter," *IEEE Trans. Power Electron.*, vol. 36, no. 1, pp. 583–596, Jan. 2021.

[24] T. Friedli, M. Hartmann, and J. W. Kolar, "The essence of three-phase PFC rectifier systems—Part II," *IEEE Trans. Power Electron.*, vol. 29, no. 2, pp. 543–560, Feb. 2014.

[25] M. F. Vancu, T. Soeiro, J. Mühlethaler, J. W. Kolar, and D. Aggeler, "Comparative evaluation of bidirectional buck-type PFC converter systems for interfacing residential DC distribution systems to the smart grid," in *Proc. 38th Annu. Conf. IEEE Ind. Electron. Soc.*, 2012, pp. 5153–5160.

[26] L. Schrittwieser, J. W. Kolar, and T. B. Soeiro, "Novel SWISS rectifier modulation scheme preventing input current distortions at sector boundaries," *IEEE Trans. Power Electron.*, vol. 32, no. 7, pp. 5771–5785, Jul. 2017.
[27] B. Zhang, S. Xie, X. Wang, and J. Xu, "Modulation method and control strategy for full-bridge-based swiss rectifier to achieve ZVS operation and suppress low-order harmonics of injected current," *IEEE Trans. Power Electron.*, vol. 35, no. 6, pp. 6512–6522, Jun. 2020.
[28] B. Zhang, S. Xie, Z. Li, P. Zhao, and J. Xu, "An optimized single-stage isolated Swiss-type AC/DC converter based on single full-bridge with midpoint-clamper," *IEEE Trans. Power Electron.*, vol. 36, no. 10, pp. 11288–11297, Oct. 2021.
[29] X. Li, J. Sun, L. Guo, M. Gao, H. Hu, and M. Xu, "A three-phase single-stage AC/DC converter based on Swiss rectifier and three-level LLC topology," *IEEE Trans. Power Electron.*, vol. 38, no. 2, pp. 1958–1972, Feb. 2023.
[30] Q. Chang, B. Zhou, C. Lu, and J. Wei, "Analysis and design of third-harmonic current injection active filter circuit for the aircraft," *IEEE Trans. Power Electron.*, vol. 39, no. 5, pp. 5764–5775, May 2024.
[31] Q. Chang, B. Zhou, C. Lu, and J. Wei, "Improved three-level third-harmonic current injection active filter circuit for the three-phase diode rectifier in aircraft," *IEEE Trans. Ind. Electron.*, vol. 72, no. 7, pp. 6604–6614, Jul. 2025.
[32] H. Wang et al., "Two-stage matrix converter based on third-harmonic injection technique," *IEEE Trans. Power Electron.*, vol. 31, no. 1, pp. 533–547, Jan. 2016.
[33] Q. Chang, B. Zhou, C. Lu, S. Jiang, and J. Wei, "A sinusoidal doubly salient electromagnetic machine drive fed by third-harmonic injection two-stage matrix converter with integrated injection inductor," *IEEE Trans. Ind. Electron.*, vol. 71, no. 4, pp. 3418–3428, Apr. 2024.
[34] Z. Guo, W. Zhan, and Z. Chen, "Single-stage isolated AC–DC converter based on LCL resonant DAB converters with single-loop control," *IEEE Trans. Power Electron.*, vol. 39, no. 8, pp. 9305–9317, Aug. 2024.
[35] G. Xu, L. Li, X. Chen, Y. Liu, Y. Sun, and M. Su, "Optimized EPS control to achieve full load range ZVS with seamless transition for dual active bridge converters," *IEEE Trans. Ind. Electron.*, vol. 68, no. 9, pp. 8379–8390, Sep. 2021.
[36] Z. Guo, "Modulation scheme of dual active bridge converter for seamless transitions in multiworking modes compromising ZVS and conduction loss," *IEEE Trans. Ind. Electron.*, vol. 67, no. 9, pp. 7399–7409, Sep. 2020.
[37] S. Mu, Z. Guo, and Y. Luo, "Universal modulation scheme to suppress transient DC bias current in dual active bridge converters," *IEEE Trans. Power Electron.*, vol. 37, no. 2, pp. 1322–1333, Feb. 2022.
[38] Z. Guo, Z. Chen, and Z. Chen, "Pareto optimum design of the magnetic components in DAB converters based on nondominated sorting genetic algorithms-II," *IEEE Trans. Power Electron.*, vol. 38, no. 10, pp. 12961–12974, Oct. 2023.
[39] N. Hou and Y. W. Li, "Overview and comparison of modulation and control strategies for a nonresonant single-phase dual-active-bridge DC–DC converter," *IEEE Trans. Power Electron.*, vol. 35, no. 3, pp. 3148–3172, Mar. 2020.

Luming Liu received the B.S. degree in electrical engineering from Anhui University of Technology, Anhui, China, in 2021, and the M.S. degree in electrical engineering from Shanghai Maritime University, Shanghai, China, in 2024. He is currently working toward the Ph.D. degree in electrical engineering with the School of Automation, Beijing Institute of Technology, Beijing, China.

His current research interests include renewable energy generation and bidirectional ac–dc converter.

Zhiqiang Guo (Senior Member, IEEE) received the B.S. degree in automation from the Hebei University of Technology, Tianjin, China, in 2008, and the M.S. and Ph.D. degrees in electrical engineering from the Beijing Institute of Technology, Beijing, China, in 2010 and 2015, respectively.

He was a Postdoctoral Research Fellow with the Department of Electrical Engineering, Tsinghua University, Beijing, China, from 2015 to 2017. In 2017, He joined the faculty of the School of Automation, Beijing Institute of Technology, Beijing, China, where he is currently an Associate Professor. He has authored more than 50 papers and two books in the field of power electronics. His current research interests include dc–dc converters, distributed generation, and microgrid applications.